

Residual stress and distortion of rectangular and S-shaped Ti-6Al-4V parts by Directed Energy Deposition: modelling and experimental calibration

Xufei Lu^{a,b}, Xin Lin^{a,b,*} xlin@nwpu.edu.cn, Michele Chiumenti^c, Miguel Cervera^c, Yunlong Hu^{a,b}, Xianglin Ji^a, Liang Ma^{a,b}, Haiou Yang^{a,b,*} yanghaiou@nwpu.edu.cn, Weidong Huang^{a,b}

^a State Key Laboratory of Solidification Processing, Northwestern Polytechnical University, Youyixilu, Xi'an, Shaan Xi 710072, P. R. China

^b Key Laboratory of Metal High Performance Additive Manufacturing and Innovative Design, MIIT China, Northwestern Polytechnical University, Youyixilu, Xi'an, Shaan Xi 710072, P. R. China

^c International Center for Numerical Methods in Engineering (CIMNE), Universidad Polit cnica de Catalu na (UPC), Edificio C1, Campus Norte, Gran Capit n s/n, 08034 Barcelona, Spain

* Corresponding author.

Abstract

Residual stresses and distortion in Additive Manufactured (AM) parts are two key obstacles which seriously hinder the wide application of this technology. Nowadays, understanding the thermomechanical behavior induced by the AM process is still a complex task which must take into account the effects of both the process and the material parameters, the microstructure evolution as well as the pre-heating strategy. One of the challenges of this work is to increase the complexity of the geometries used to study the thermomechanical behavior induced by the AM process. The reference geometries are a rectangular and a S-shaped structures made of 44-layers each. The samples have been fabricated by Directed Energy Deposition (DED). In-situ thermal and distortion histories of the substrate are measured in order to calibrate the 3D coupled thermo-mechanical model. Once the numerical results showed a good agreement with the temperature measurements, the validated model has been used to predict the residual stresses and distortions. Different process parameters have been analyzed to study their sensitivity to the process assessment. Different preheating strategies have been also analyzed to check their effectiveness on the mitigation of both distortions and residual stresses. Finally, some simplifications of the actual scanning sequence are proposed to reduce the computational cost without loss of the accuracy of the simulation framework.

Key words: Residual stress; distortion; Directed Energy Deposition (DED); Complex structure; Thermomechanical simulation.

1 Introduction

Directed Energy Deposition (DED) is one of the several Additive Manufacturing (AM) technologies used for advanced free form fabrication in which the metal powder is spread coaxially with the laser (or electron beam) input [1,2]. The powder is melted within the melt-pool and quickly solidifies and consolidates to the substrate or to the previously deposited layer. Although the advantages of DED are widely accepted, distortions and residual stresses still are two of the key issues that hinder the wide application of this technology in the industry. The localized heating due to the moving heat source and the following uneven cooling in DED process induce large thermal gradients. These thermal gradients provoke the formation of both residual stresses and distortions reducing of the mechanical strength and the geometrical accuracy of the fabricated components. Hence, the reduction of residual stresses and distortions in DED is a crucial aspect to qualify both the manufacturing process and the fabricated components.

The thermo-mechanical modeling based on the finite element (FE) method is adopted to effectively predict the thermo-mechanical behavior of the metal deposition during the AM process and to determine the optimal processing parameters for the mitigation of deformations and residual stresses of the built [3,4]. In AM, several numerical models have been proposed to predict the thermal history [5-10] and the mechanical response of the parts [11-17]. Chew et al. [18] developed a 3D thermo-mechanical model to analyze the laser cladding and they validated their model by comparing the residual stresses of single bead by the X-ray diffraction measurements. The experimental measurements are in agreement with their numerical results, but the model is restricted to a single layer laser cladding. Denlinger et al. [17,19-21] developed a model using the code CUBIC by Pan Computing LLC to predict the accumulation of both distortion and residual stresses of AM parts. In-situ thermal and distortion histories at the bottom surface of the substrate have been measured together with the residual stresses to improve the accuracy of the model. They concluded that once the temperature is higher than the stress relaxation temperature (690°C), it is extremely important to take into account the stress annealing to achieve good agreement with the experimental evidence. However, the evolution of the thermo-mechanical fields in AM are poorly discussed without discussing the sensitivity to the annealing temperature in Ti-6Al-4V. Zhao et al. [22] developed a model for EBAM in ANSYS to study the annealing temperature due to the Solid State Phase Change (SSPC) of the Ti-6Al-4V; they finally fixed it to 850°C using different temperature XRD measurements. Because of the non-unique definition of the constitutive laws for the characterization of the material behavior used to simulate the mechanical response of the AM parts, the value of the annealing temperature needs to be deepened. Ding et al. [23-24] found that the maximum temperature achieved during the WAAM process is one key factor affecting the generation of the residual stresses in the built. Based on this, they develop a simplified steady-state model where the peak temperature determines the stress evolution. Although the computational time reduced of almost 80%, the proposed method is accurate only when large parts are analyzed. In fact, the steady-state approximation introduces significant errors in case of small size parts [25].

Although different numerical methods have been reported in literature to deal with the thermomechanical analysis of the AM process, most of them focus their studies on simple AM structures. One of the key objectives of this work is to extend the analysis to more complex geometries such as the proposed rectangular and S-shaped models while keeping the accuracy of the fully coupled thermo-mechanical simulation framework with the high-fidelity reproduction of the metal deposition sequence.

The reduction of the residual stresses and distortions is the second main challenge of this work. Taking advantage

from the expertise gained in welding, Chin et al. [26,27] showed that increasing the initial temperature of the substrate just before the metal deposition process together with an enhanced mechanical constraining can reduce both residual stresses and distortions. However, the preheating strategy is not analyzed in the case of complex geometries. Corbin et al. [28] showed that the substrate preheating mitigates the deformation in thin substrate but increases the distortion of thick ones. However, the relationship between the substrate thickness and the preheating procedure is not quantified. Some further studies [29-31] indicate that the use of rolling processes in Wire-feeding by Arc Additive Manufacturing (WAAM) is helpful to mitigate the residual stresses.

This given, the objective of this work is to study the evolution and mitigation of residual stresses and distortions induced by the DED technology for Ti-6Al-4V when complex rectangular and S-shaped parts are fabricated. Firstly, a 3D coupled thermo-mechanical FE software is used to predict the thermomechanical behavior of Ti-6Al-4V parts fabricated by DED technology. The optimization of both process and material parameters for Ti-6Al-4V suitable for thermomechanical modeling of DED was presented in our previous work [11]. The software is further validated in our Labs using a DED machine to fabricate different parts by varying the process parameters. The relationship between the actual parameters and the modeling strategy is discussed in detail. Secondly, using the validated model, different preheating strategies and cooling rates are analyzed to prove their influence of on the mitigation of both residual stresses and distortions. Finally, the simplification of the actual deposition strategy used to reduce the computational cost in AM simulation is proposed.

2 DED modeling

Firstly, a 3D transient thermal analysis is performed to calibrate the temperature field according to the heat absorption characterizing the DED process and the heat dissipation through the surrounding environment. Next, a fully coupled thermo-mechanical analysis is performed to predict the evolution of both the stress and strain fields as well as the distortions of the builds. Note that the energy input from the laser source is much higher than the plastic dissipation (negligible) so that the problem is weakly coupled (one way coupling). Hence, a staggered solution arising from a fractional step method is preferred to the monolithic approach. In this section, the governing equations and the constitutive laws of both the thermal and the mechanical problems are briefly summarized. A more detailed description modelling strategy for AM has been presented in previous work of the authors [5,11,13,32].

The FE analyses are performed using the *Comet* software developed at the International Center for Numerical Methods in Engineering (CIMNE) [33]. The GiD pre-post-processor [34] is used for the CAD design, the mesh generation and the results post-processing.

2.1 Transient thermal analysis

The transient energy balance equation to compute the heat transfer analysis in the whole volume of the component is:

$$\dot{H} = -\nabla \cdot \mathbf{q} + \dot{Q} + \dot{D}_{mech} \quad (1)$$

where \dot{H} is the rates of enthalpy, \dot{Q} is the heat source and \dot{D}_{mech} is the thermomechanical dissipation. The heat flux \mathbf{q} is computed through the Fourier's law as:

$$\mathbf{q} = -k\nabla T \quad (2)$$

where k is the temperature dependent thermal conductivity.

Newton's law of cooling states that the heat loss due to the heat convection, q_{conv} , is:

$$q_{conv} = h_{conv}(T - T_{env}) \quad (3)$$

where h_{conv} is the heat transfer coefficient by convection, T is the temperature on the surface of the part, and T_{env} is the ambient temperature.

The heat radiation is computed using Stefan-Boltzmann's law:

$$q_{rad} = \varepsilon_{rad}\sigma_{rad}(T^4 - T_{env}^4) \quad (4)$$

where ε_{rad} is the surface emissivity, σ_{rad} is the Stefan-Boltzmann constant.

2.2 Mechanical analysis

The balance of momentum equation characterize the mechanical problem used for the stress analysis:

$$\nabla \cdot \boldsymbol{\sigma} + \mathbf{b} = 0 \quad (5)$$

where $\boldsymbol{\sigma}$ is the Cauchy stress tensor and \mathbf{b} are the body forces.

The mechanical constitutive law is defined as:

$$\boldsymbol{\sigma} = \mathbf{C} : \boldsymbol{\varepsilon}_e \quad (6)$$

where \mathbf{C} is the fourth order elastic constitutive tensor. The elastic strains, $\boldsymbol{\varepsilon}_e$, are calculated as:

$$\boldsymbol{\varepsilon}_e = \boldsymbol{\varepsilon} - \boldsymbol{\varepsilon}_p - \boldsymbol{\varepsilon}_T \quad (7)$$

where $\boldsymbol{\varepsilon}$, $\boldsymbol{\varepsilon}_p$ and $\boldsymbol{\varepsilon}_T$ are the total, the plastic and the thermal strains, respectively. The specific thermo-visco-elasto-visco-plastic constitutive model for AM used in this work is detailed in references [13, 32]. The stress relaxation induced by phase transformation has been taken into account and the corresponding annealing temperature is set to 850°C [20, 22].

2.3 Rectangular and S-shaped models

Two geometries are considered in this work: a rectangular deposition 70 mm long and 30 mm wide, and a S-shaped deposition defined by an inner radius of 20 mm (see Fig. 5). Both depositions consist of 44 layers. Fig. 1 presents the FE meshes of both the rectangular and the S-shaped geometries used for the model calibration through experiments. The mesh in Fig.1(a) fits to the actual geometry of the metal deposition (conformal mesh) while the S-shaped geometry uses a non-conformal mesh as shown in Fig.1(b): according to the scanning sequence, only the elements belonging to the actual geometry (see Fig. 5) are activated to be computed and assembled into the computational model. The mesh of the rectangular deposition consists of 57,880 Q1P0 hexahedral 8-noded elements and 71,391 nodes. The mesh of the S-shaped deposition consists of 107,280 Q1P0 hexahedral 8-noded elements and 120,131 nodes. There are 4 elements placed across the laser beam diameter and 1 element per layer thickness. The sensitivity analysis addressing the use similar mesh densities has been presented in [5], and also discussed in [11,20]. Note that the mesh of the base plate is coarsened far from the deposition, guaranteeing the result accuracy of the solution, while reducing the computation cost.

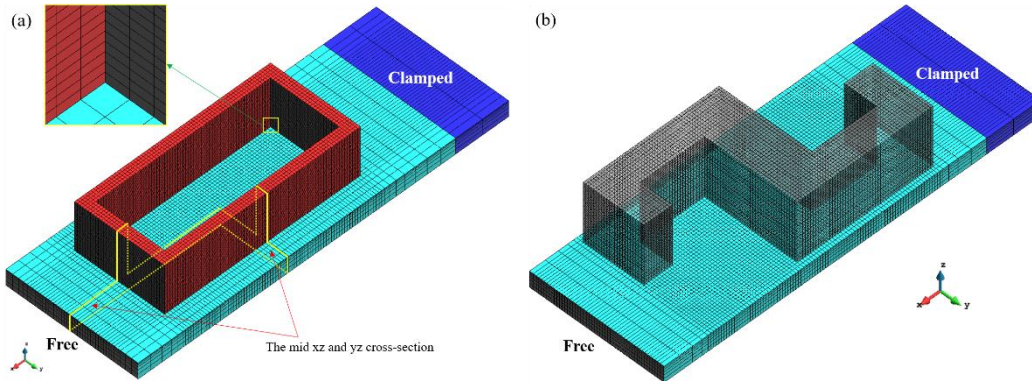


Fig.1. FE meshes used for the numerical simulation of the AM process: (a) rectangular deposition; (b) S-shaped deposition.

2.4 Material properties of Ti-6Al-4V

Table 1 lists the temperature-dependent material properties of the Ti-6Al-4V alloy used in the analyses of both components [35]. For temperatures above the melting point, the heat conductivity is increased to take into account the heat convection flow inside the melting pool. The values of the material properties in the full temperature range are obtained by the linear interpolation among the values reported in the table. Note that, the thermophysical properties of the base-plate are the same as used for the metal deposition.

Table 1 Temperature-dependent material properties of Ti-6Al-4V.

Temperature (°C)	Density (kg/m ³)	Thermal Conductivity (W/(m·°C))	Heat Capacity (J/(kg·°C))	Poisson's Ratio	Thermal Expansion Coefficient (μm/m/°C)	Young's Modulus (GPa)	Elastic Limit (MPa)
20	4420	7	546	0.345	8.78	110	850
205	4395	8.75	584	0.35	10	100	630
500	4350	12.6	651	0.37	11.2	76	470
995	4282	22.7	753	0.43	12.3	15	13
1100	4267	19.3	641	0.43	12.4	5	5
1200	4252	21	660	0.43	12.42	4	1
1600	4198	25.8	732	0.43	12.5	1	0.5
1650	3886	83.5	831	0.43	12.5	0.1	0.1
2000	3818	83.5	831	0.43	12.5	0.01	0.01

2.5 Boundary conditions

The base-plate is clamped as a cantilever by prescribing all movements at the lower and upper surfaces (see Fig.1). Both heat radiation and heat convection conditions are applied to all the external surfaces of the base-plate and the metal deposition. The heat transfer coefficient by convection for DED process of Ti-6Al-4V is set to 1 [W/m²·°C], while the emissivity parameter is set to 0.285. The value of the heat transfer coefficient by conduction at the contact interface between the base-plate and the supporting structure takes into account the thermal inertia of this supporting structure avoiding its computation. By correlating experimental and numerical results, the heat transfer coefficient used for the Newton's model is set to 50 [W/m²·°C]. The environment temperature is 25°C. Finally, the energy absorption coefficient, η , is set to 0.3. The values of all the material and processing parameters used in the model are obtained through the experimental measurements and the numerical calibration as described in following Section.

3 Experimental procedure

3.1 Experimental setup

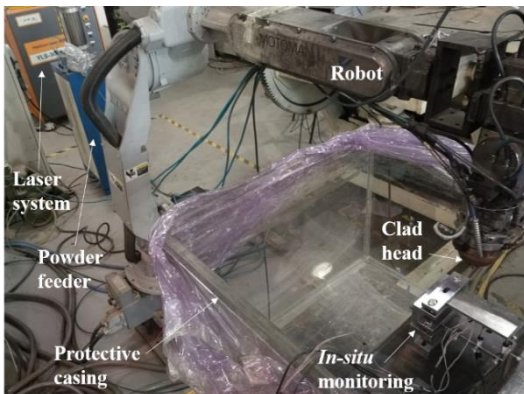


Fig.2. Directed energy deposition (DED) system.

DED technology is employed to fabricate five components on Ti-6Al-4V annealed substrates of $140 \times 50 \times 6 \text{ mm}^3$. Plasma Rotating Electrode Processed (PREP) Ti-6Al-4V powder with a spherical particle size between 53 and 150 μm is used for the metal deposition (blown powder). The powder is dried in a vacuum oven at 150°C for 2h before DED. Fig. 2 shows the DED system using a YLS-3000 IPG Photonics fiber laser with a wavelength ranging between 960~1200 nm. A maximum power of 3 kW can be applied in a close chamber filled with argon to prevent the oxidation during the DED process. The energy beam generates 4 mm spot at the component surface. A Gaussian beam profile is used to distribute the total energy through the spot surface.

Fig. 3 shows the scanning sequence adopted to build the rectangular model: the deposition makes use of 4 different sequences repeated every 4 layers.

The reciprocating scanning strategy is adopted to manufacture the S-shaped model.

Table 2 shows three different sets of process parameters used to fabricate the rectangular shape by DED. In the case of the S-shaped deposition, the only the process parameters of Case-1 and Case-2 have been adopted. The up-lift height has been adjusted to match the actual feeding rate at constant scanning speed.

In the case of the rectangular geometry the final height of the built was 21.56 mm, 18.48 mm and 12.32 mm with a wall width of 4.8 mm, 4 mm and 4 mm, respectively, according to the 3 sets of process parameters described in Table 2. For the S-shaped geometry the final height was 22.48mm and 20.68 mm while the wall width was 5.4 mm and 4 mm, according to the Case-1 and Case-2 process parameters in Table 2.

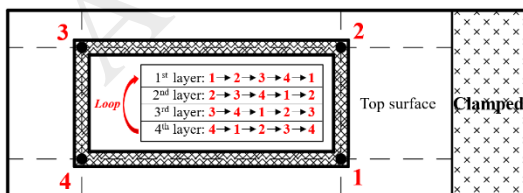


Fig.3. Schematic of the laser path order during DED process.

Table 2 Processing parameters of DED.

Case	Power input (W)	Scanning speed (mm/s)	Up-lift height (mm)	Feeding rate (g/min)
1	1500	10	0.45	12.0
2	1000	10	0.4	12.0
3	1000	10	0.25	8.0

3.2 In situ deposition measurement

In situ distortion of the base-plate during the DED process is monitored by two Displacement Sensors (DS), as shown in Fig. 4. The DS used in this work is WXXY PM11-R1-20L, with measurement accuracy of 0.02% and a maximum range of 20 mm. The vertical displacements to two points on the bottom surface of the base-plate is recorded, as shown in Fig. 5. Similarly, *in situ* temperature is measured at different locations on the bottom surface of the base-plate (see Fig. 5) using Omega GG-K-30 type K thermocouples with a measurement uncertainty of 2.2°C or 7.5%. The thermocouple and the displacement signals are recorded using a Graphtec GL-900 8 high-speed data-logger.

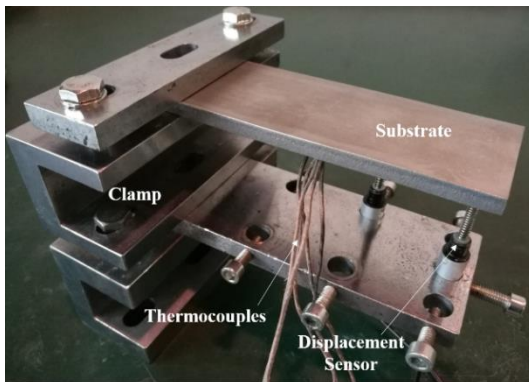


Fig.4. Experimental setup to measure the vertical displacements and temperatures of the base-plate during the DED process.

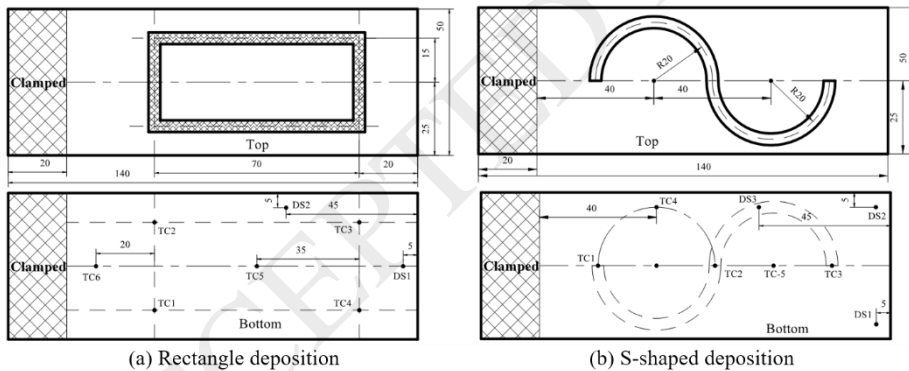


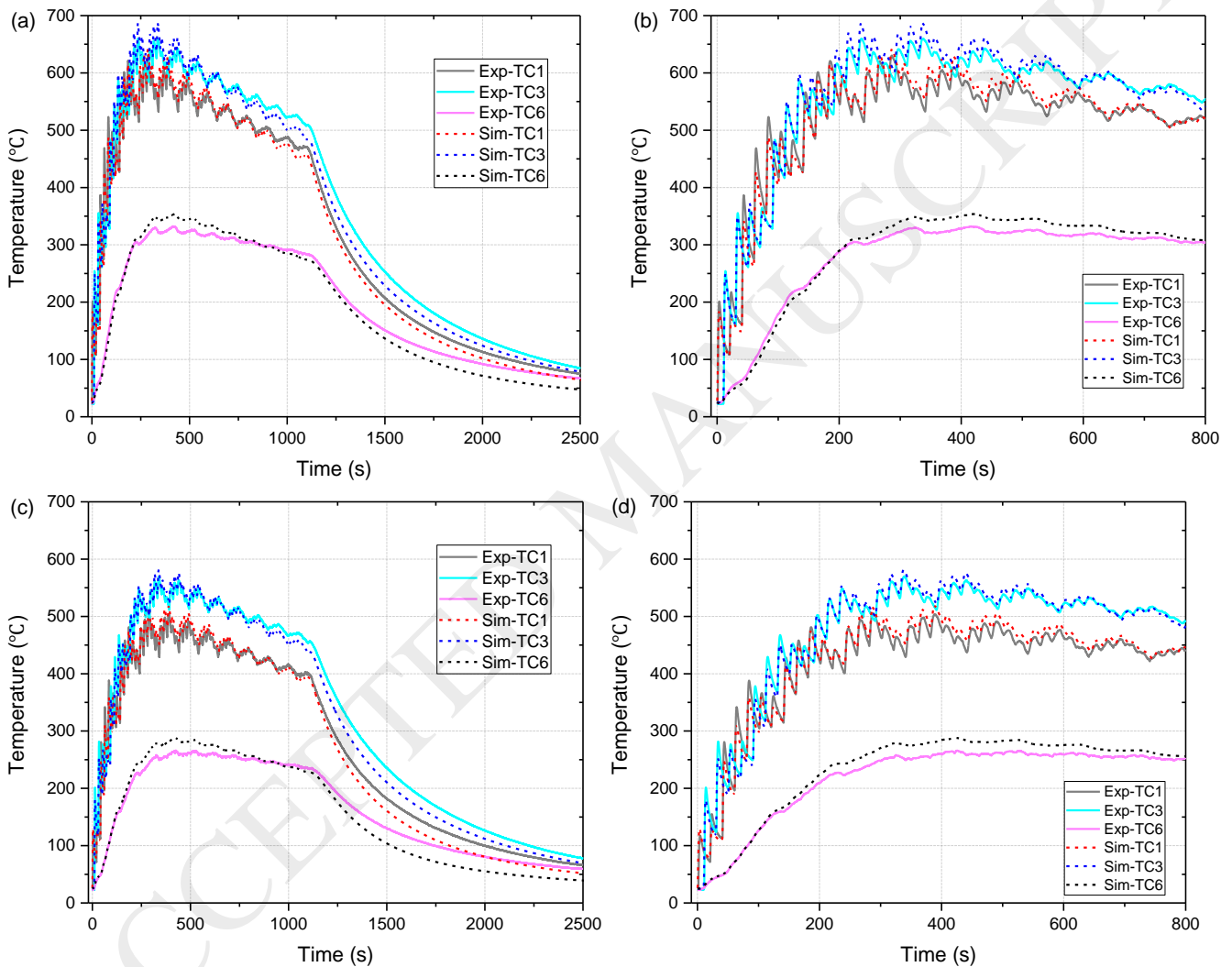
Fig.5. Sample dimensions and location of the thermocouples and displacement sensors (Unit: mm).

4 Results and discussion

4.1 Temperature history

The thermal history of the base-plate is simulated and compared to the experimental measurements. Fig. 6 and Fig. 7 show the thermal histories at the different thermocouple locations of the base-plate (see Fig. 5) of the rectangular and S-shaped depositions, respectively. The data are obtained through the simulation and the experimental measurements during the actual manufacturing, respectively. A remarkably good agreement is achieved.

In the DED process, the evolution of the temperature can be split in 3 phases. Firstly, the base-plate is rapidly heated up by the heat input from the room temperature up to the peak temperature. This temperature exceeds 650°C, 550°C and 600°C when depositing the 10th, 12th and 12th layer, respectively. It can be seen from Fig. 6 that the peak temperature measured at TC3 is about 80°C higher than the value at TC1. The second stage corresponds to the deposition of the remaining layers till completing the built. The sample temperatures begin to decrease gradually due to the larger distance of the heat source from the base-plate according to the growing of the part. After the deposition process is completed, the laser input is switched off and the substrate quickly cools down. During the deposition process, both the simulated and the experimental curves show the fluctuations resulting from the regular scanning movement of the laser along the scanning path. Due to the increasing distance from the substrate, this amplitude slowly reduces.



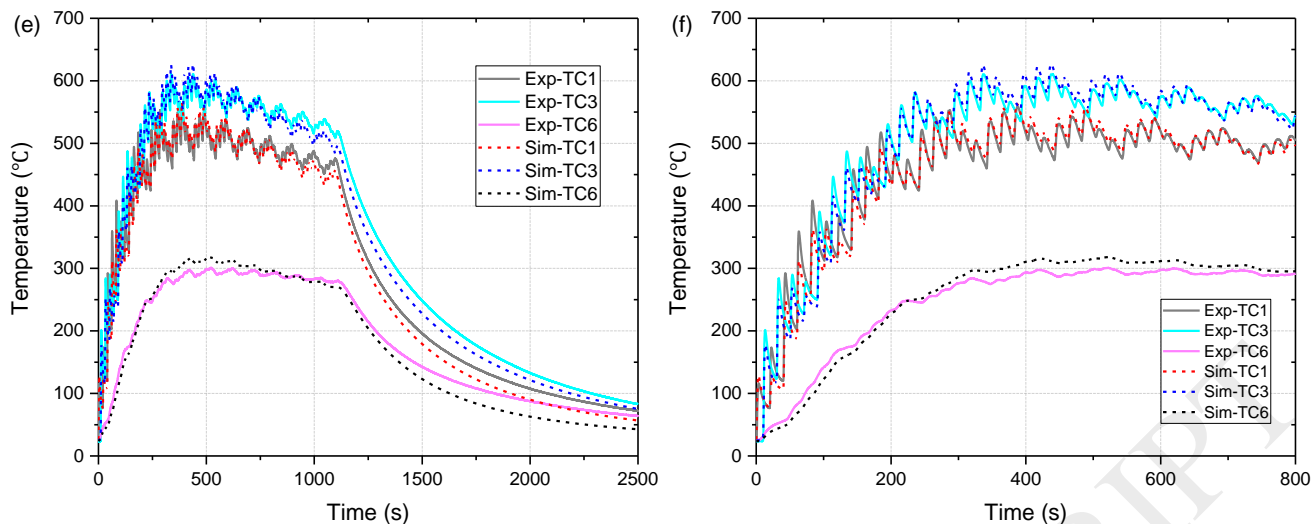


Fig.6. Comparison between the calculated and recorded thermal history of the rectangular metal depositions at each thermocouple according to different process parameters: (a) and (b) Case 1; (c) and (d) Case2; (e) and (f) Case3.

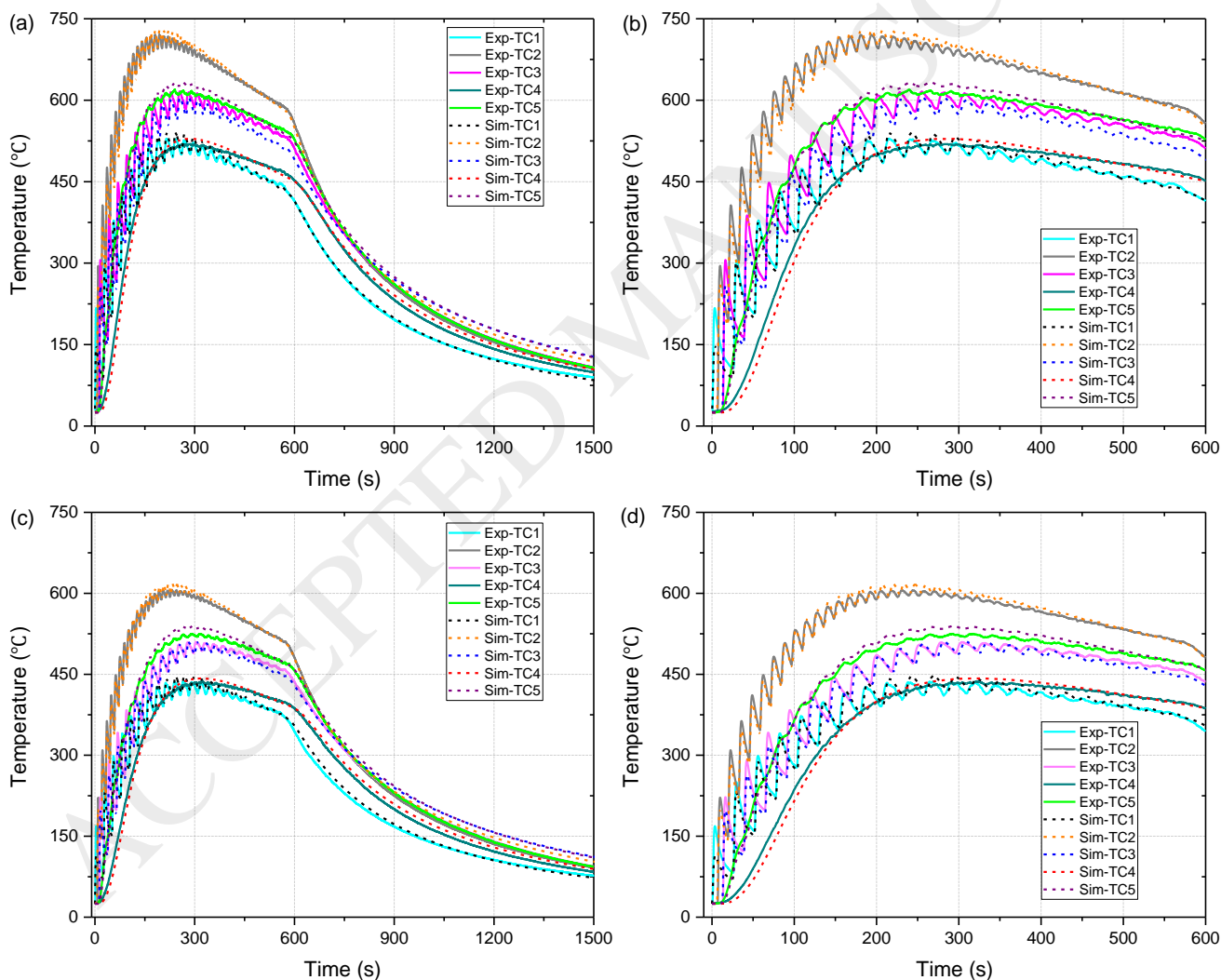


Fig.7. Comparison between the calculated and monitored thermal history of the S-shaped depositions at each thermocouple according to different process parameters: (a) and (b) Case 1; (c) and (d) Case2.

It can be seen that increasing the laser power, the higher mass input leads to higher peak temperatures as well as larger temperature fluctuation amplitudes, respectively.

Similar temperature evolutions at the different thermocouples placed on the S-shaped model can be observed in Fig. 7. Note that the time needed for reaching the peak temperature for the S-shaped samples is larger and corresponds to the deposition of the 20th layer.

There is a slight mismatch between the numerical and experimental results due to the simplification of the thermal boundary conditions in the DED process. A possible reason for this is that there is a non-negligible part of the powder which is accumulated into the melt pool. Similar results have been published by Denlinger et al. [20] showing that the temperature of the sample increases for roughly the first third of the build and then starts to decrease due to the incremented penetration of melt-pool for higher temperature of the built.

The average error in the whole calculation for each case can be calculated as:

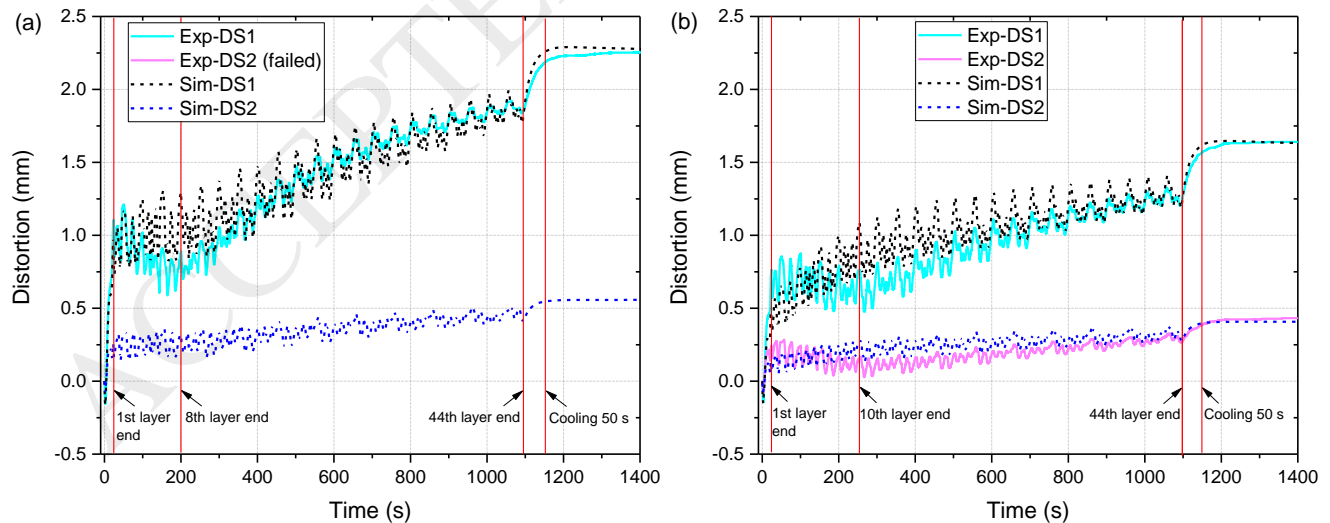
$$\%Error = \frac{100 \sum_{i=1}^n \frac{|(x_{exp})_i - (x_{sim})_i|}{(x_{exp})_i}}{n} \quad (8)$$

where n is the number of simulated time increments between the beginning and ending of the deposition, i is the current time increment, x_{exp} is the measured temperature, and x_{sim} is the corresponding simulated temperature. The errors at the different thermocouple locations are shown in Table 3 are less than 12.74% for all cases.

Table 3 The average error of the temperature evolution.

Case	%Error TC1	%Error TC3	%Error TC6	%Error TC1	%Error TC2	%Error TC3	%Error TC4	%Error TC5
	Rectangular deposition			S-shaped deposition				
1	4.98	4.82	10.46	3.72	4.94	6.83	4.55	5.88
2	8.67	5.97	12.74	2.97	4.75	5.98	4.31	6.04
3	7.40	6.56	12.51					

4.2 Distortion history



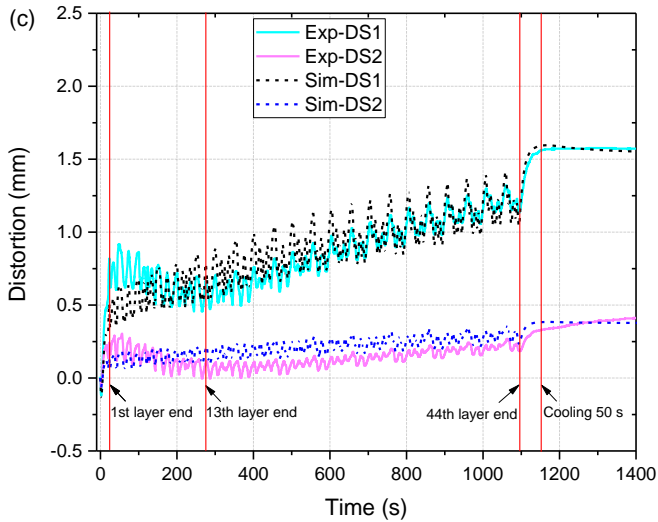


Fig.8. Comparison between the calculated and measured distortions of rectangular depositions at each DS for different process parameters: (a) Case 1; (b) Case 2; (c) Case 3.

The vertical displacements at the DS locations of the rectangular deposition are calculated and compared to the experimental measurements during DED using different process parameters. Fig. 8 shows the evolution of the vertical displacements of rectangular deposition obtained from calculations and experiments at locations DS1 and DS2 of the base-plate (as presented in Fig. 5(a)).

The distortion history for each case can be split into 4 phases. During the deposition of the 1st layer, the thermal dilatation of the upper surface of the substrate yield to the generation plastic deformations. This initial displacement is about 0.15 mm downward. After that, the cooling and shrinking of the metal deposition results in a sharp upward displacement of about 1 mm upward. This first phase is the responsible of about 50% of the total distortions. The reason for that is that large thermal gradients induced by the heat source on the cold base-plate provoke the large distortion. During the deposition going from the 2nd to the 8th layers (in Case 1), the distortions of the substrate is gradually reduced from 1.2 mm to 0.7 mm, as shown in Fig.8(a). The temperature of the substrate ranges from 380°C at the end of the 2nd layer to 650°C for the 8th layer, corresponding to the end of this stage (see Fig. 6(a)). When the temperature of the Ti-6Al-4V alloy reaches the alpha-beta phase transformation (between 600~980°C), the transformations strains are opposed to the thermal strain due to the contraction of the molten material [20]. Hence, the corresponding thermal softening results in a stress relaxation and then a reduction of the substrate distortions. During the deposition of the remaining layers (from 9th to 44th) till finishing the part, the distortion of the substrate increases again. The average value of the distortion is proportional to the temperature of the base-plate (see Fig.6(a)). In the final cooling stage, the deformation of the substrate rapidly increases up to 0.5 mm within 50 s; thus almost 25% of the total distortion is developed at the beginning of the cooling stage without changing very much during the rest of the cooling phase.

Note that, when the laser power is increased by 50% (Case 1 vs. Case 2), the final residual distortion is also increased by 40%. Contrarily, when the powder feeding is increased by 50% (Case 2 vs. Case 3), the final residual distortion is increased by 3%, only. Hence, increasing the heat input has a significant impact on the distortion of the substrate while changing the powder feeding almost does not affect the residual distortion.

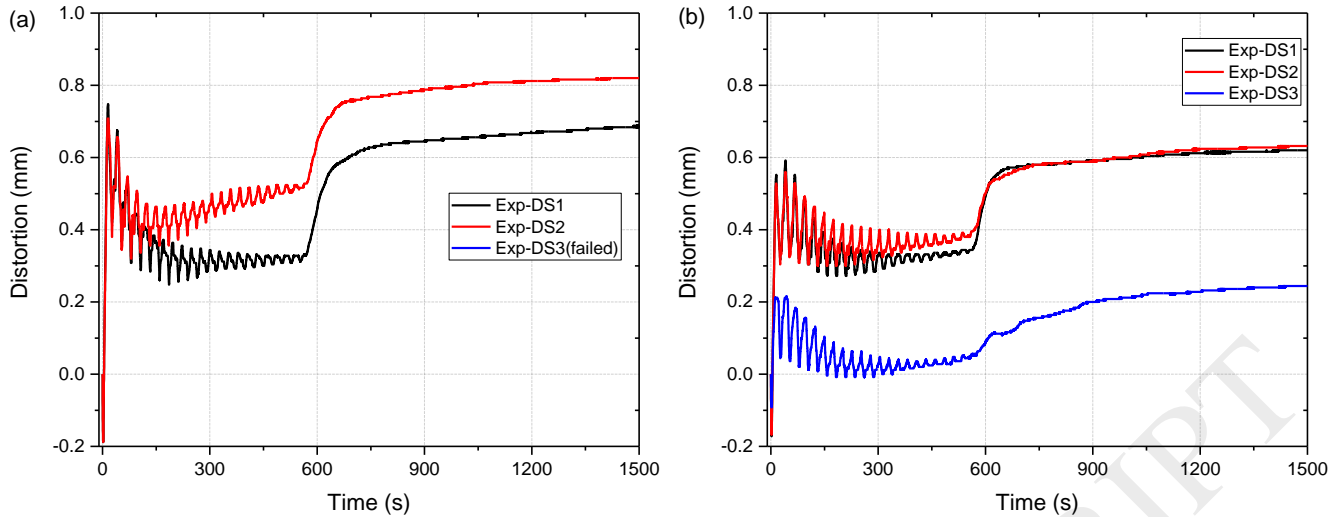


Fig.9. Comparison between the calculated and measured distortions of S-shaped depositions at each DS for different process parameters: (a) Case 1; (b) Case 2

Fig. 9 shows the experimental measurements of the longitudinal bending evolution of the S-shaped depositions at each DS (see Fig. 5(b)). Observe that there are many similarities with the evolution of the distortion of the rectangular depositions, such as the sharp increases of the longitudinal bending during the deposition of the first layer and during the final cooling phase. However, after the deposition of the 2nd layer the vertical displacements quickly reduce and then holds nearly constant during the remaining deposition process. The reason for this is that the temperature field of the S-shaped part is above 500°C throughout the subsequent deposition (see Fig. 7). This issue guarantees the thermal softening of the entire base-plate leading to a significant reduction (less than 0.81mm) of the bending induced by the initial deposition. Note that, when the laser power is increased by 50%, a distortion in the transversal direction (0.13 mm) appears, which indicates that the lack of symmetry of this structure affects significantly the mechanical responses of both distortion and residual stresses.

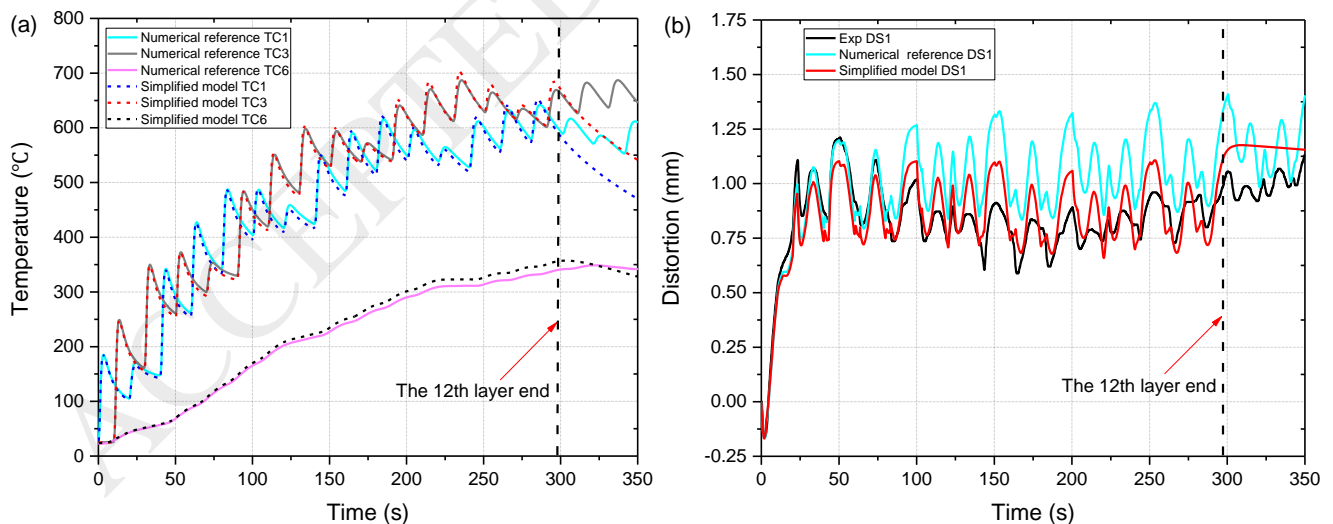


Fig.10. Rectangle depositions: thermo-mechanical evolution of Case 1 with decreasing the initial layer thickness: (a) Temperature; (b) Deformation.

During the initial deposition process, a slight mismatch between the numerical and experimental distortion is appreciable in Fig. 8. One possible reason for this is that the model considers a constant average thickness of the

deposited layers (final height of the built divided by the total number of layers). However, in the initial phase of the DED process, the heat input in the molten pool is rapidly absorbed by the cold substrate, and so the actual dimensions of the molten pool are reduced, leading to a smaller layer thickness during the initial metal deposition process. After the deposition of the following layers, the temperature of the substrate is gradually increased and the balance between the heat input and heat dissipation reaches the steady state. Hence, the temperature field within the molten pool reaches a dynamic stability in terms of shape, size and maximum temperature. Thus, the effective thickness and width of the deposited layer also gradually increase and stabilize during the DED process.

In order to verify the above hypothesis, a simplified model with only 12 layers is considered. The thickness of each layer is set to 0.35 mm (while the average thickness is 0.49 mm for Case 1) keeping all the other model parameters unchanged. Fig. 10 shows the comparison of both the temperature and distortion between the numerical reference and the simplified model. It can be seen that the difference between the two temperature curves is negligible, while the distortion is notably improved in the simplified model. This demonstrates that the thickness of the first layers is actually smaller than the average thickness during the steady state conditions, and its impact on the mechanical response is remarkable. Note that the distortion evolution in the more advanced phase of the metal deposition process is in good agreement with the experimental measurements (see Fig. 8).

Fig. 11(a) shows the predicted deformation for the manufactured rectangular deposition for Case 1 and Fig. 11(b) shows the corresponding experimental data. The residual deformation is measured in terms of the final bending of the substrate. The deformation predicted by the model is 2.63 mm, which is in good agreement with the experimental measurement of 2.61 mm.

Based on the above analyses, the large thermal gradients in the initial phase of the metal deposition and the high cooling rates in final cooling phase are the responsible for the residual distortion. Moreover, this distortion is also strongly influenced by the geometry and the process parameters selected. In particular, it turns out that increasing the initial temperature of the substrate before the metal deposition and controlling the cooling rate once the built is terminated are the key factors to reduce the longitudinal bending of the base-plate. Finally, to mitigate the transverse distortion (e.g. for the S-shape geometry) it is necessary to optimize the process parameters and particularly the laser power and scanning speed.

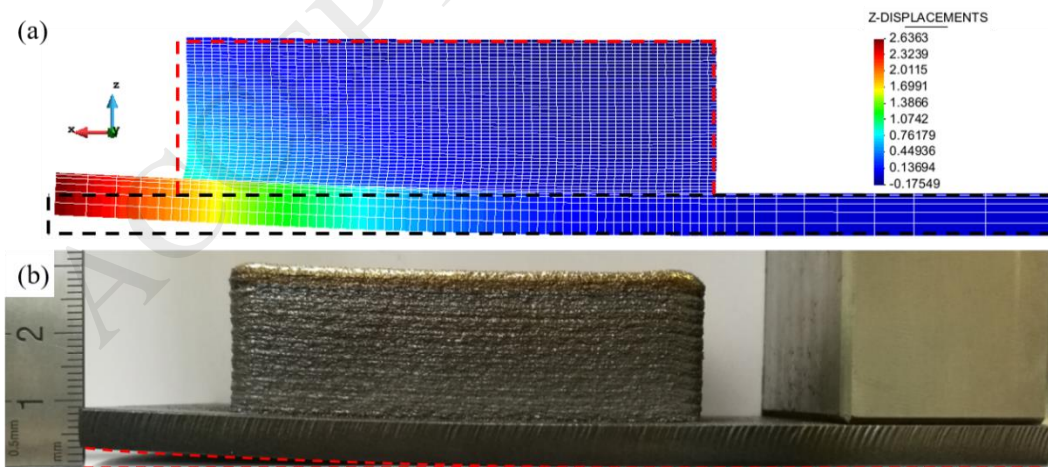


Fig.11. Rectangular deposition: Comparison of simulation predicted distortion of case 1 with experimental result.

4.3 Stress fields

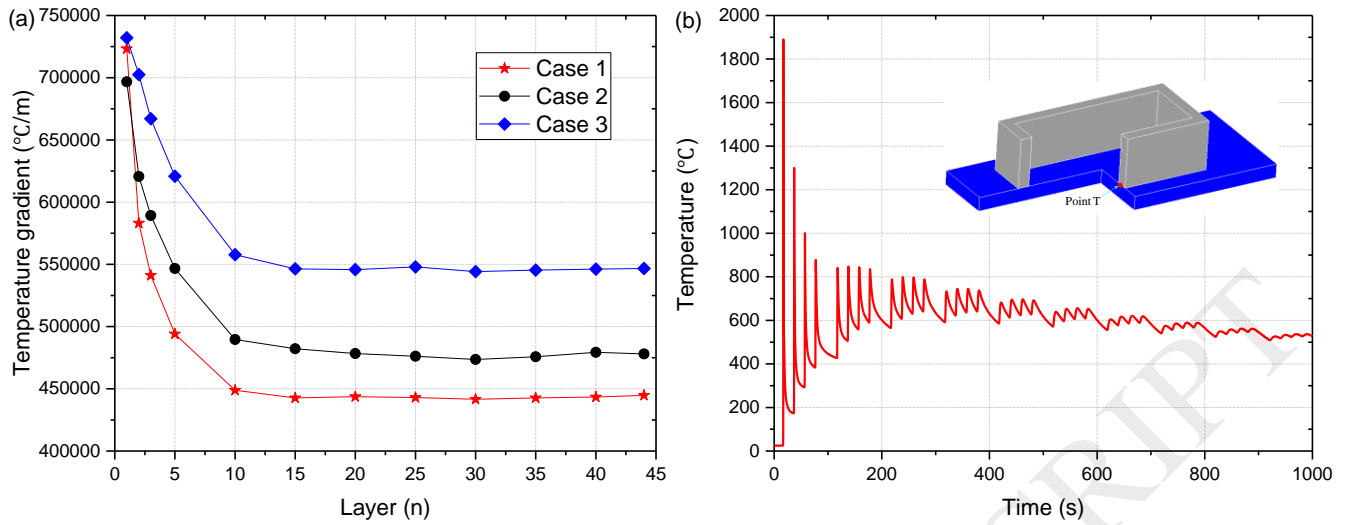


Fig. 12. Thermal evolution of the rectangular deposition: (a) maximum thermal gradients along the scanning direction according to the deposition sequence; (b) thermal history of point T under Case 1.

In this section, the evolution of the stress field of the rectangular deposition for Case 1 is analyzed. In order to assess the thermomechanical response induced by the DED process, the maximum thermal gradients along the scanning direction and the thermal history of the point T are shown in Fig. 12. Fig. 12(a) shows that the maximum thermal gradient is about 7.25×10^5 °C/m and corresponds to the deposition of the first layer (the substrate is cold at the beginning of the DED process). By increasing the number of the deposited layers, the maximum thermal gradient gradually reduces, to stabilize after the deposition of the 10th layer according to the temperature increase of the substrate (see Fig. 6). When the powder feeding is reduced (Case 2 vs. Case 3), the heat absorption for the metal deposition is remarkably reduced leading to an increase of the melt-pool temperature. Hence, the thermal gradient for Case 2 is larger than for Case 3. In addition, the thermal curve, shown in Fig. 12(b), generates a sharp fluctuation in the first few layers and then tending to steady, which indicates that a very inhomogeneous thermal distribution is provoked in initial stage due to the high energy input and the cold base-plate. These severe temperature changes induce notably the generation and development of the stresses and distortion.

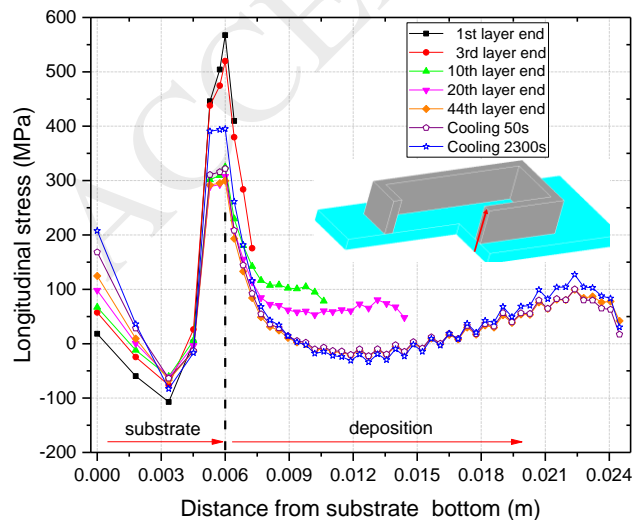


Fig. 13. Rectangular deposition: calculated stress (σ_{xx}) at the mid yz cross-section under Case 1 during the DED process.

The longitudinal stresses (σ_{xx}) along the direction of the deposition at the mid yz cross-section are shown in Fig. 13. In this figure, it can be seen that after the deposition of the 1st layer, a maximum tensile stress of 560 MPa is generated at the interface between the base-plate and the metal-deposition together with a compressive stress (-150 MPa) in the middle of the substrate. This is due to the large thermal gradient and the rapid cooling and shrinkage of the built. According to the reduction of the thermal gradient during the deposition of the first 10 layers, the tensile stresses at the bottom of the deposition reduce significantly. After the deposition of the 10th layer, the tensile stresses remain unchanged close to the value of 300 MPa. In the cooling phase, the maximum tensile stress increases up to 400 MPa, that is, to 25% of the maximum residual stress. Note that most of the layers far away from the base-plate show a lower level of residual stress.

The evolution of the longitudinal stresses in the walls for Case 1 at different process times is shown in Fig. 14. Fig. 14(a) and (b) show that, after the deposition of the 1st layer, the rapid cooling and the shrinkage of this layer result in the plastic deformation due to the thermal contraction of the top surface of the substrate near the deposition (see Fig. 12(b)). This contributes to increase the distortion of the substrate (see Fig. 8). At the same time, there exist large longitudinal tensile stresses along the scanning direction for both the shorter and the longer walls, reaching values up to 700 MPa. The transversal stresses are very small due to the stiffness of the walls under construction. After the deposition of the 2nd layer, the longitudinal tensile stresses on the top of the walls along the scanning direction clearly decrease, due to the quick increasing of the substrate temperature and the reduction of the thermal gradient. The maximum tensile stresses occur at the interface between the base-plate and the metal-deposition. Continuing the manufacturing process, the cooling and shrinkage of the different layers provoke a slight increase of the compressive stresses at the upper surface of the substrate. After the deposition of the 10th layer, the temperature field becomes more uniform while the level of the stresses is reduced. When the deposition of all the layers is finished, the thermal contraction of the entire structure results in the mechanical compression of the upper surface of the substrate while the bottom surface is subjected to tensile stresses up to 300 MPa, leading to bending of the base-plate at the end of the metal deposition process (see Fig. 8).

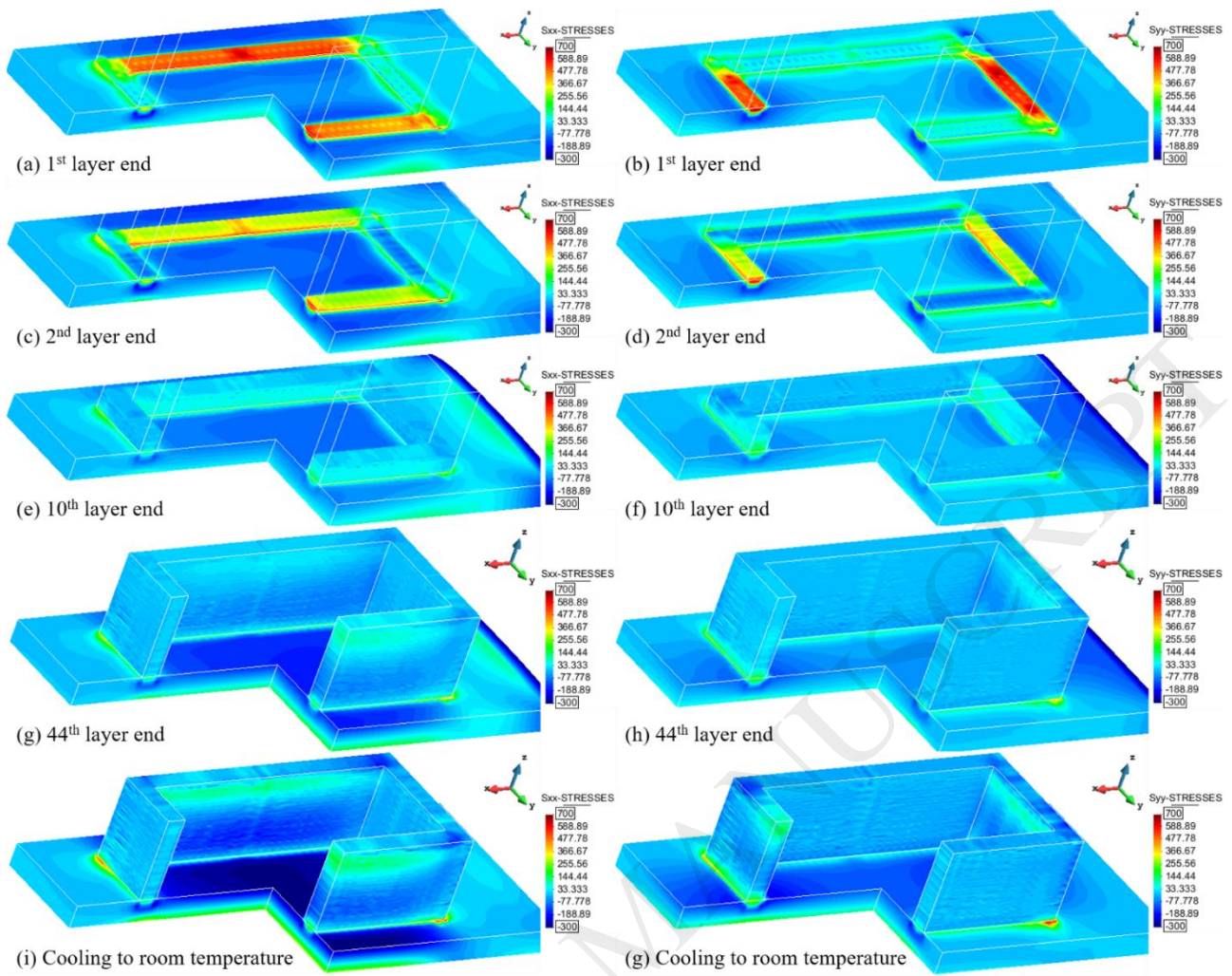


Fig. 14. Rectangular deposition: the evolution of the stresses field under Case 1 for different process times: (a), (c), (e), (g), (i) longitudinal stress (σ_{xx}) for the longer walls; (b), (d), (f), (h), (g) the longitudinal stress (σ_{yy}) for the shorter walls.

Fig. 15 shows the longitudinal residual stress distributions for the long and the short walls along the red and yellow lines on the top of the substrate (see Fig. 15). Observe that the large tensile stresses (σ_{xx} and σ_{yy}) in the longitudinal direction reach values up to 400 and 480 MPa, respectively. However, the longitudinal residual stresses within the rectangle are compressive with values up to -200 MPa. The sharp cooling and shrinkage of the rectangular deposition during the final cooling phase are the main responsible for this (see Fig. 6). From the numerical analyses, the actual dimensions of the rectangular deposition are smaller than the nominal geometry due to the shrinkage of the entire structure during the cooling phase.

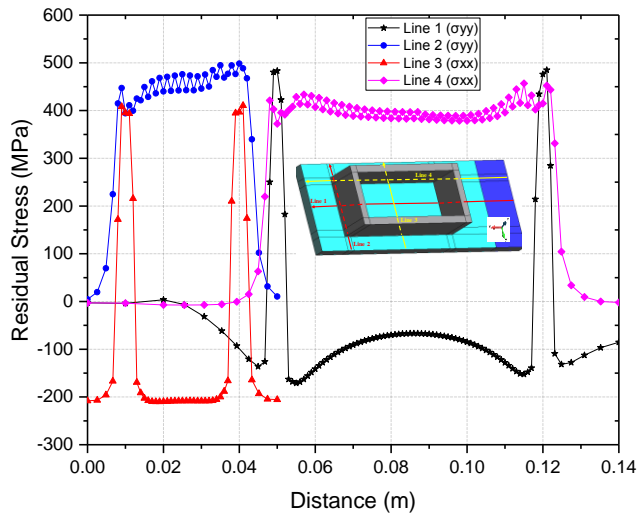


Fig. 15. Rectangular deposition: calculated longitudinal residual stresses (σ_{xx} and σ_{yy}) along the scanning direction according to the deposition sequence.

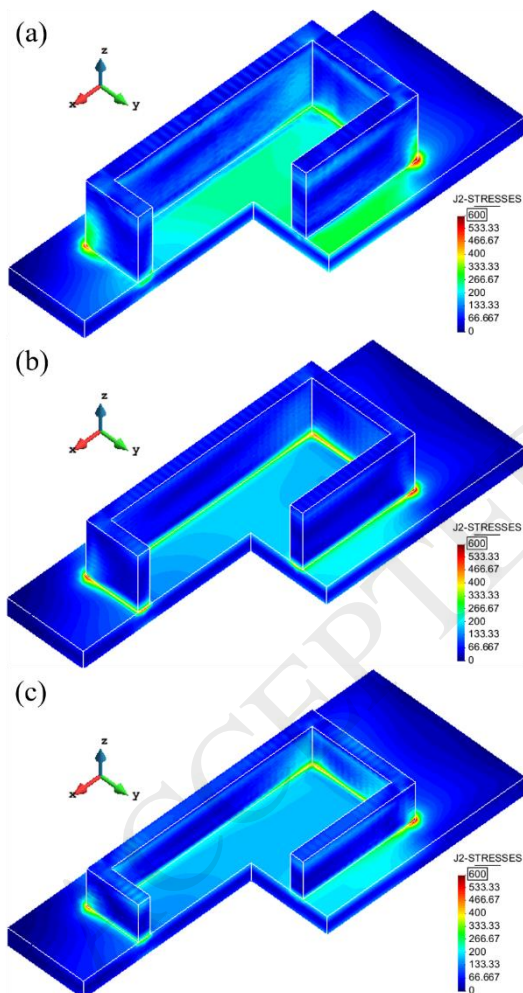


Fig.16. Rectangular deposition: calculated residual von Mises stresses: (a) Case 1, (b) Case2, (c) Case3.

The calculated von Mises residual stresses for each case at the room temperature are shown in Fig. 16. It can be seen that the larger stresses occur at the interface between the base and the deposition. In particular, the largest residual stresses (600 MPa) are located at the corners of the walls due to the higher thermal gradients induced by the local heat

accumulation at these points. Although the residual stress distribution is similar for all cases, higher heat input (Case 1) induces the largest residual stresses; especially the compressive stresses at the upper surface of the base-plate (see Figs. 14 and 16). Moreover, increasing the powder feeding by 50% (Case 2 vs. Case 3) has little effect on the residual stress field. These results are consistent with the conclusions obtained in section 4.2.

By analyzing the evolution of the longitudinal stresses during the WAAM process of a single-wall discussed by Ding et al. [23] also reported in [36-38], it is found that large thermal gradients and high cooling rates are two key factors for the generation and development of distortions and stresses, independently of the heat sources used (laser, electron beam or arc) or the clamping condition of the substrate. In particular, the maximum value of the longitudinal residual stresses is concentrated at the interface between the substrate and wall, while decreasing towards the top of the wall. The rectangular and the S-shaped depositions present some similarities with the thermo-mechanical behavior of the single-wall presented by Ding et al. [23]. Nevertheless, increasing the complexity of the fabricated components makes their thermo-mechanical behavior more intricate. In particular, the heat diffusion process and heat losses depend on the scanning strategy (power input, feeding rate, deposition sequence, etc.), size and shape of the selected components. The differences in the temperature field influence the local material strength and the global stiffness of the structure. Hence, studying more complex geometries, while preserving the accuracy of the simulation framework, is important to analyze the effects induced by the process parameters.

5 The influence of preheating and cooling rate on the mechanical field

It is possible to reduce residual stresses by preheating the substrate [28,37]. The effectiveness of this method must be proven for relatively complex structures. Therefore, different preheating strategies and cooling rates are examined to find the optimal method to mitigate both the deformation and the residual stresses. Fig. 17 shows three different scanning paths used for the DED: (1) spiral pattern defined by three cycles; (2) transversal pattern, in which the laser moves parallel to the shorter walls; (3) longitudinal pattern, in which the laser moves parallel to the longer walls. Next, different pre-heating temperatures used to heat the whole substrate are also discussed: 400 °C, 500 °C, 600 °C and 700 °C, respectively.

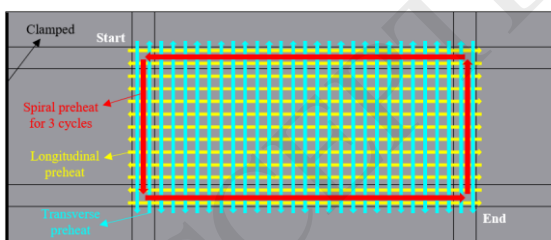


Fig.17. Rectangular deposition: different scanning strategies of laser preheating used in Case 1.

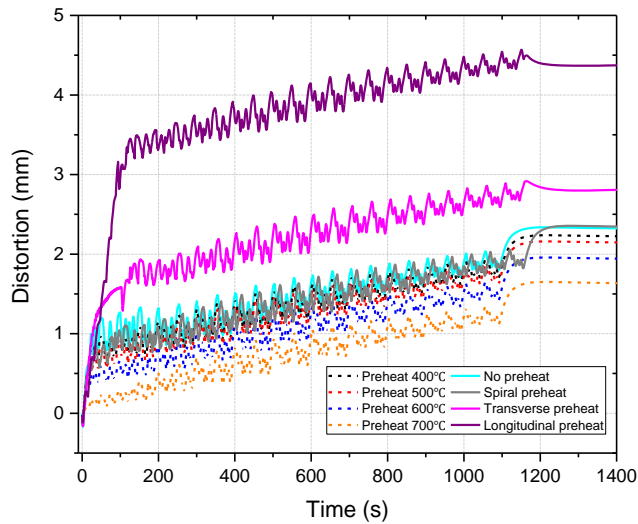


Fig.18. Rectangular deposition: the predicted distortion at the DS1 of the substrate under different preheating conditions.

The substrate distortions due to different preheating conditions for the process parameters of Case 1 are shown in Fig. 18. A significant variation of the substrate distortion is due to the use of different scanning paths. The use of longitudinal preheating is the worst resulting in a maximum distortion of 3 mm. The best solution consists of using the spiral path leading to a more uniform temperature field for the whole substrate.

By increasing the preheating temperature of the whole substrate can reduce the residual deformation. In particular, when the temperature is about 700 °C, the initial deformation of the substrate almost vanishes. The reason for this is that increasing the preheating temperature of the whole substrate, the thermal gradients during the initial deposition reduces correspondingly. Although the distortion due to the deposition of the first layers can be alleviated, it can develop in the subsequent deposition process and, particularly, during the cooling phase.

The simulated longitudinal residual stresses using different preheating conditions at the top surface of the substrate are shown in Fig. 19. The results show that the preheating can mitigate effectively the residual stresses. For three different scanning patterns, the longitudinal preheating is the most effective method to mitigate the tensile stress at the interface between the substrate and the deposition. However, the transversal and longitudinal preheating result in larger compressive stresses (up to -600 MPa) at the edges of the substrate. When the preheating temperature is set to 700°C, the material is softened and the residual tensile stress at the bottom of the deposition is less than 60 MPa.

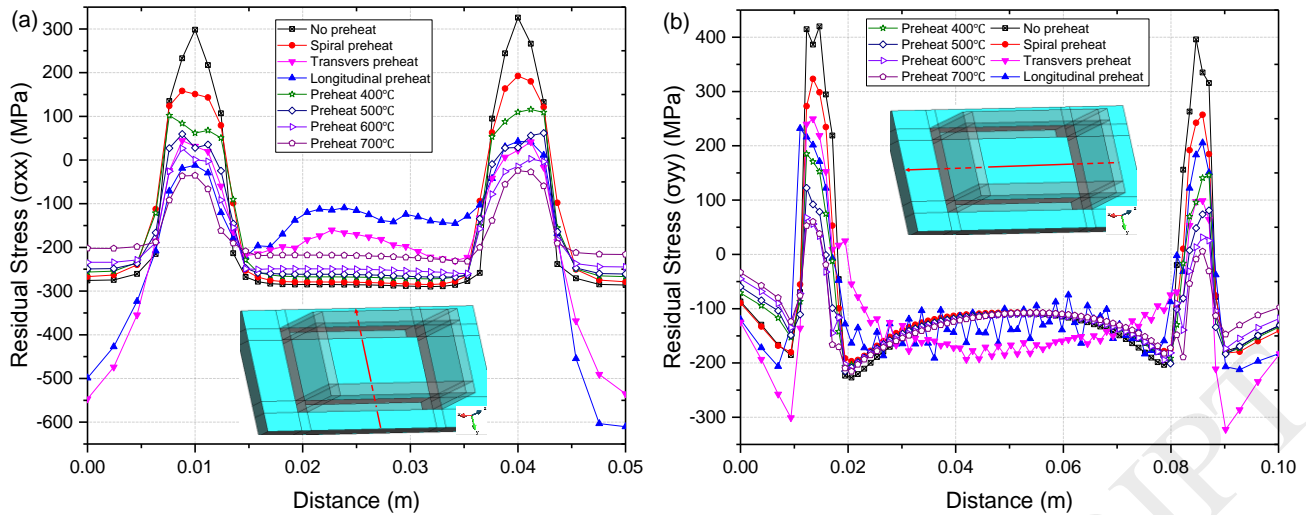


Fig. 19. Rectangular deposition: calculated longitudinal residual stress at the top surface of the substrate for different preheating conditions: (a) paralleling the longer walls; (b) paralleling the shorter walls.

Fig. 20 shows the influence of the cooling rate of the deposition on the mechanical response of the built for Case 1. In this analysis, the initial temperature of the substrate is set to 700°C and the ambient temperature decreases uniformly from 400°C (or 500°C) to 25°C in 3 hours in the final cooling phase. It can be seen from Fig. 20(a) that when increasing the ambient temperature, that is, when decreasing the temperature gradients of the deposition, the distortion induced by the manufacturing process is effectively mitigated. When the ambient temperature reaches 500°C, the maximum distortion during the depositing process and the final distortion does not exceed 0.025 mm and 0.5 mm, respectively. It can be seen from Fig. 20(b) that the residual von Mises stresses of the deposition when the ambient temperature is 500°C are very small. The maximum value is less than 100 MPa.

The mitigation of the maximum residual tensile stress and the final deformation applying the different preheating strategies and cooling rates is shown in Table 4. When the preheating temperature of the whole substrate is about 700°C and the ambient temperature is kept at 500°C in the DED process, the final deformation and residual stresses are mitigated by 90.1% and 80.2%, respectively.

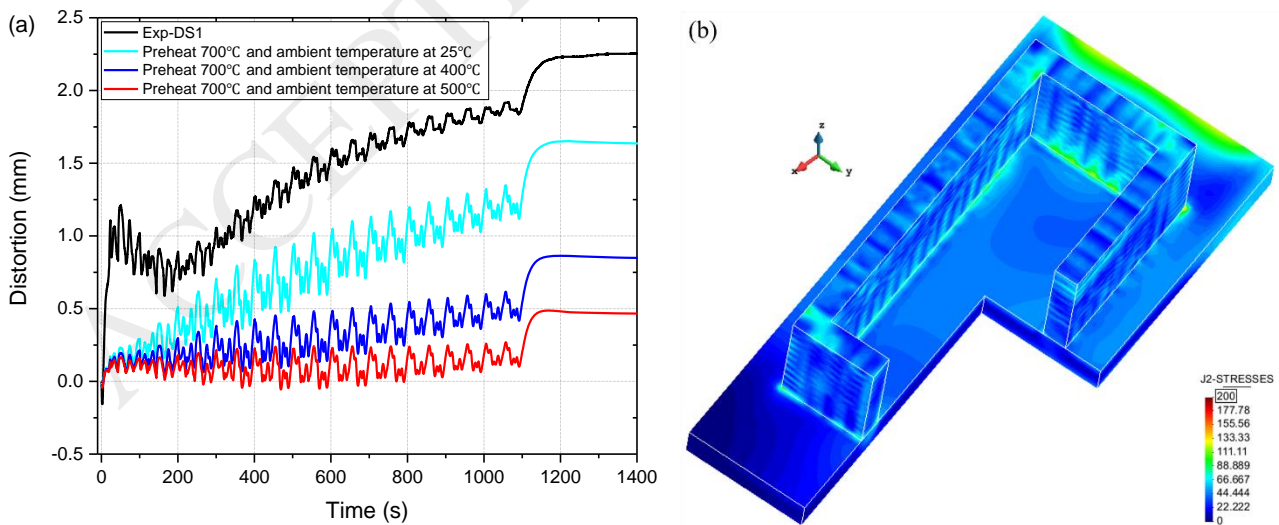


Fig. 20. Rectangular deposition: calculated mechanical responses of the build under Case 1: (a) distortion for different cooling rates; (b) residual von Mises stresses for ambient temperature at 500 °C.

Table 4 Reduction of distortion and maximum residual tensile stress under Case 1 for different preheat conditions and cooling rates.

	Spiral preheat	Transverse preheat	Longitudinal preheat	Preheat 400°C	Preheat 500°C	Preheat 600°C	Preheat 700°C	T _{ambient} at 400 °C	T _{ambient} at 500 °C
Distortion (%)	-0.8	-21.1	-88.3	3.9	5.2	15.9	29.3	63.4	80.2
Residual stress (%)	22.8	39.7	45.2	55.7	70.4	80.3	85.2	87.3	90.1

6 Simulation speed-up

There exist many simplified methods to speed-up the simulation time. In the case of powder-bed technologies such as the Selective Laser Melting (SLM), the use of the inherent strain methods [39-40] drastically reduce computational time by completely decoupling the stress analysis from the thermal diffusion process. This is possible because of the thin size of the layers, the use of low energy input and the recoating time (while spreading a new powder layer the whole temperature of the component drops below the annealing temperature). This is not the case when using the DED technology. Hence, the strategy proposed is based on the simplification of the scanning sequence: the problem is solved by a fully coupled method but the activation strategy can be reduced to a layer-by-layer sequence. In this work a 4-layer-by-4-layer activation strategy has been selected to further enhance the CPU-time while preserving the global trend of the simulation.

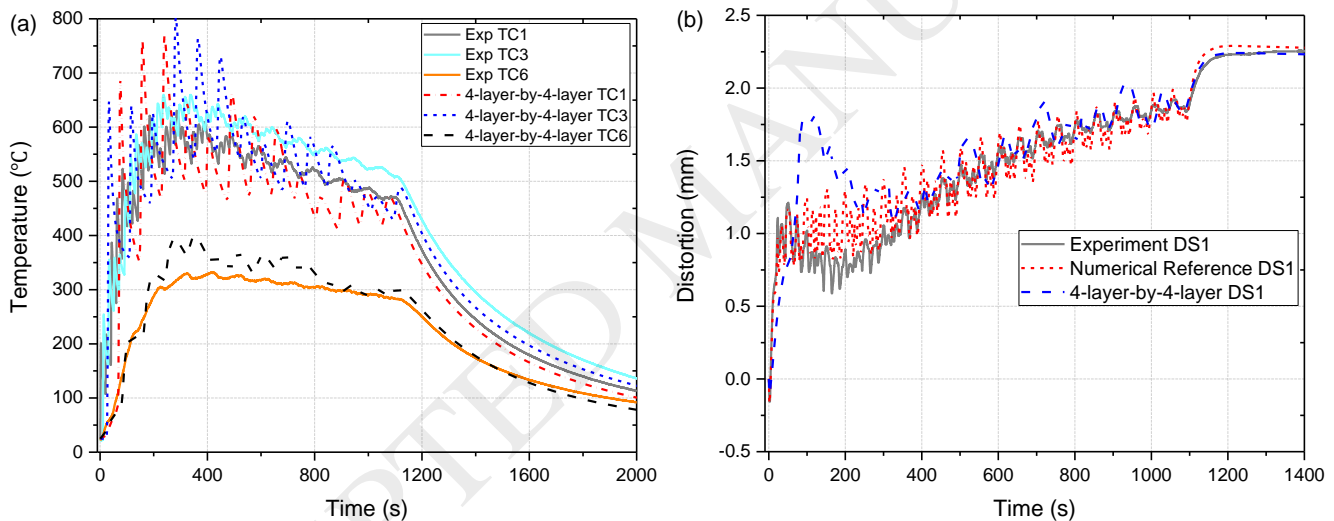


Fig. 21. Rectangular deposition: numerical results of obtained by 4-layer-by-4-layer strategy under Case 1: (a) thermal history; (b) distortion.

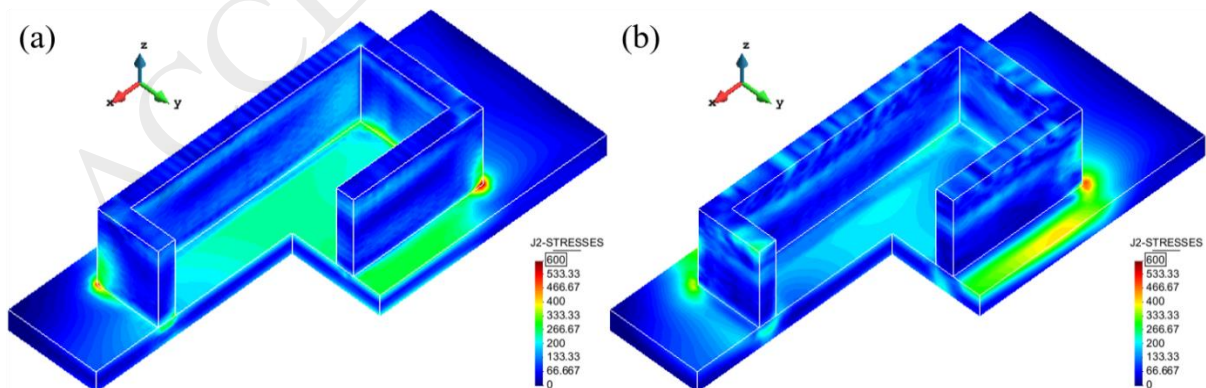


Fig. 22. Numerical results of residual von Mises stresses filed under Case 1: (a) numerical reference; (b) using 4-layer-by-4-layer strategy.

Hence, at each time step, the elements belonging to the next 4 layers are activated, using an equivalent scanning rate

of 2.5 mm/s. Fig. 21 and Fig. 22 show the numerical results obtained. Even if large oscillations of the thermal field can be observed in Fig. 21(a), the average value as obtained by the experimental data is preserved.

Fig. 21(b) shows a large mismatch of the displacements (more than 1 mm) due to the use of this simplified strategy just after the deposition of the first 4-layers. However, during the following metal deposition and cooling phases, the distortion calculated using the 4-layer-by-4-layer activation strategy agrees well with the experimental results and the numerical reference. The simplification of the scanning strategy affects the thermal distribution at the beginning of the process when the temperature gradients due to the cold substrate are smoothed; when approaching the steady-state conditions, the thermomechanical behavior is less sensitive to the scanning strategy adopted.

Note that there still exist some differences in the residual stress field. Even if the global average stiffness of the structure is preserved, the stresses are affected by the local conditions (peak temperature and temperature gradients), as shown in Fig. 22.

This simplified strategy leads to a reduction of the CPU-time of 77%. Hence, depending on the simulation accuracy required, the 4-layer-by-4-layer activation strategy is an efficient way to get a fast prediction the thermomechanical behavior of the metal deposition by DED.

7 Conclusion

In this paper, a 3D thermo-mechanical FE model is calibrated to study both distortions and residual stresses induced by DED. The sensitivity to the process parameters is analyzed. One of the challenges of this work consists of studying complex geometries while preserving the accuracy of the computational framework. Once validated, the model has been used to explore different preheating and cooling strategies as well as their sensitivity on the final residual stresses and distortions.

The samples have been manufactured using the DED technology while monitoring both the temperatures and distortions through in-situ measurements.

The main conclusions of this work are the following:

- 1) The computed temperature field is in good agreement with the experimental results. The maximum average error at all thermocouple locations is less than 12.74%.
- 2) The use of a constant layer thickness to model the deposition all layers generates a small mismatch in the first part of the distortion curve. Contrarily, in DED process, the layer thickness gradually increases from the initial small value (because of the cold substrate) to reach an almost constant value during the following depositions. Hence, the use of a variable layer thickness should be adopted to optimize the model accuracy in DED process.
- 3) The complexity of the geometry has a significant impact on the mechanical behavior if compared to simpler and smaller depositions. This is due to the more intricate heat diffusion which modifies the local strength of the material and the global stiffness of the structure. The unsymmetrical stress distribution induced by the S-shaped model is a clear example of the geometrical effects of the components, leading to a large transversal distortion up to 0.13 mm.
- 4) The stresses and distortion is strongly affected by the heat input but poorly affected by the powder feeding rate. Thus, controlling the heat input (laser power and scanning speed) is an efficient strategy to mitigate both residual distortion and residual stresses.

- 5) The substrate preheating can reduce the residual stresses but may increase the final distortion (up to 88.3% in the analyzed geometries). Contrarily, increasing the preheating temperature of the whole base-plate and decreasing the cooling rate at the end of the deposition can remarkably mitigate both the residual stresses and distortions. When the preheating temperature reaches 700°C and the ambient temperature is kept at 500°C, the residual stresses and final distortion are reduced of 80.2% and 90.1%, respectively. The use of different scanning strategies in the preheating phase has an important effect on the distortion. The more uniform is maintained the temperature (spiral strategies), the better is the final result.
- 6) The CPU-time can be reduced by 77% by using a 4-layer-by-4-layer activation strategy. The local accuracy of the simulation (local temperatures, stress field) is affected by this simulation strategy but the average values of both temperature and stiffness/distortion are preserved.

Acknowledgements

This work was supported by National Key Technologies R & D Program (Nos. 2016YFB1100100 and 2016YFB1100602) and National Natural Science Foundation of China (Nos. 51323008 and 51475380). Funding from the Spanish Ministry of Economy and Competitivity under the ADaMANT project: *Computational Framework for Additive Manufacturing of Titanium Alloy Components* (ref: DPI2017-85998-P), within the Excellency Programme for Knowledge Generation is gratefully acknowledged.

References

- 1 Guo N, Leu M C. Additive manufacturing: technology, applications and research needs [J]. *Frontiers of Mechanical Engineering*, 2013, 8(3): 215-243.
- 2 Gibson I, Rosen D, Stucker B. *Additive Manufacturing Technologies*[M]. Springer US, 2010..
- 3 Wang Z, Denlinger E, Michaleris P, et al. Residual stress mapping in Inconel 625 fabricated through additive manufacturing: Method for neutron diffraction measurements to validate thermomechanical model predictions[J]. *Materials & Design*, 2017, 113: 169-177.
- 4 Wang Z, Stoica A D, Ma D, et al. Diffraction and single-crystal elastic constants of Inconel 625 at room and elevated temperatures determined by neutron diffraction[J]. *Materials Science and Engineering: A*, 2016, 674: 406-412.
- 5 Chiumenti M, Lin X, Cervera M, et al. Numerical simulation and experimental calibration of Additive Manufacturing by blown powder technology. Part I: thermal analysis[J]. *Rapid Prototyping Journal*, 2017, 23(2): 448-463.
- 6 Kolossov S, Boillat E, Glardon R, et al. 3D FE simulation for temperature evolution in the selective laser sintering process[J]. *International Journal of Machine Tools and Manufacture*, 2004, 44(2): 117-123.
- 7 Peyre P, Aubry P, Fabbro R, et al. Analytical and numerical modelling of the direct metal deposition laser process[J]. *Journal of Physics D*, 2008, 41(2).
- 8 Sammons P M, Bristow D A, Landers R G. Height dependent laser metal deposition process modeling[J]. *Journal of Manufacturing Science and Engineering*, 2013, 135(5): 054501.
- 9 Shen N, Chou K. Thermal Modeling of Electron Beam Additive Manufacturing Process. *Powder Sintering Effects*[J]. ASME Paper No. MSEC2012-7253, 2012.
- 10 Jamshidinia M. Numerical Modeling of Heat Distribution in the Electron Beam Melting of Ti-6Al-4V[J]. *Journal of Manufacturing Science & Engineering*, 2013, 135(6):61010-61011.
- 11 Lu X, Lin X, Chiumenti M, et al. Finite element analysis and experimental validation of the thermomechanical behavior in laser solid forming of Ti-6Al-4V[J]. *Additive Manufacturing*, 2018, 21: 30-40.
- 12 Andrés A, Fachinotti V D, Gustavo E, et al. Computational modelling of shaped metal deposition[J]. *International Journal for Numerical Methods in Engineering*, 2011, 85(1):84-106.
- 13 Chiumenti M, Cervera M, Salmi A, et al. Finite element modeling of multi-pass welding and shaped metal deposition processes[J]. *Computer Methods in Applied Mechanics & Engineering*, 2010, 199(37-40):2343-2359.
- 14 Marimuthu S, Clark D, Allen J, et al. Finite element modelling of substrate thermal distortion in direct laser additive manufacture of an aero-engine component[J]. *Proceedings of Institution of Mechanical Engineers Part C Journal of Mechanical Engineering Science*, 2013, 227(9):1987-1999.
- 15 Lundbäck A, Lindgren L E. Modelling of metal deposition[J]. *Finite Elements in Analysis & Design*, 2011, 47(10):1169-1177.
- 16 Yang Q, Zhang P, Cheng L, et al. Finite element modeling and validation of thermomechanical behavior of Ti-6Al-4V in directed energy deposition additive manufacturing[J]. *Additive Manufacturing*, 2016, 12: 169-177.
- 17 Denlinger E R, Heigel J C, Michaleris P. Residual stress and distortion modeling of electron beam direct manufacturing Ti-6Al-4V[J]. *Proceedings of the Institution of Mechanical Engineers, Part B: Journal of Engineering Manufacture*, 2015, 229(10): 1803-1813.
- 18 Chew Y, Pang J H L, Bi G, et al. Thermo-mechanical model for simulating laser cladding induced residual stresses with single and multiple clad beads[J]. *Journal of Materials Processing Technology*, 2015, 224: 89-101.
- 19 Heigel J C, Michaleris P, Reutzel E W. Thermo-mechanical model development and validation of directed energy deposition additive manufacturing of Ti-6Al-4V[J]. *Additive manufacturing*, 2015, 5: 9-19.
- 20 Denlinger E R, Michaleris P. Effect of stress relaxation on distortion in additive manufacturing process modeling[J]. *Additive Manufacturing*, 2016, 12: 51-59.
- 21 Denlinger E R, Irwin J, Michaleris P. Thermomechanical modeling of additive manufacturing large parts[J]. *Journal of Manufacturing Science and Engineering*, 2014, 136(6): 061007.

- 22 Chen Z, Ye H, Xu H. Distortion control in a wire-fed electron-beam thin-walled Ti-6Al-4V freeform[J]. *Journal of Materials Processing Technology*, 2018.
- 23 Ding J, Colegrove P, Mehnen J, et al. A computationally efficient finite element model of wire and arc additive manufacture[J]. *International Journal of Advanced Manufacturing Technology*, 2014, 70(1-4):227-236.
- 24 Ding J, Colegrove P, Mehnen J, et al. Thermo-mechanical analysis of Wire and Arc Additive Layer Manufacturing process on large multi-layer parts[J]. *Computational Materials Science*, 2011, 50(12):3315-3322.
- 25 Shangvi J Y, Michaleris P. Thermo- elasto- plastic finite element analysis of quasi- state processes in Eulerian reference frames[J]. *International Journal for Numerical Methods in Engineering*, 2002, 53(7):1533-1556345.
- 26 Chin R, Beuth J, Amon C. Control of residual thermal stresses in shape deposition manufacturing[C]//*Proceedings of the Solid Freeform Fabrication Symposium*, Austin, TX, Aug. 1995: 221-228.
- 27 Klingbeil N W, Beuth J L, Chin R K, et al. Residual stress-induced warping in direct metal solid freeform fabrication[J]. *International Journal of Mechanical Sciences*, 2002, 44(1): 57-77.
- 28 Corbin D J, Nassar A R, Reutzel E W, et al. Effect of Substrate Thickness and Preheating on the Distortion of Laser Deposited Ti-6Al-4V[J]. *Journal of Manufacturing Science and Engineering*, 2018, 140(6): 061009.
- 29 Colegrove P A, Coules H E, Fairman J, et al. Microstructure and residual stress improvement in wire and arc additively manufactured parts through high-pressure rolling[J]. *Journal of Materials Processing Technology*, 2013, 213(10): 1782-1791.
- 30 Martina F, Roy M J, Colegrove P A, et al. Residual stress reduction in high pressure interpass rolled wire+ arc additive manufacturing Ti-6Al-4V components[C]//*Proc. 25th Int. Solid Freeform Fabrication Symp.* 2014: 89-94.
- 31 Hönnige J R, Williams S, Roy M J, et al. Residual stress characterization and control in the additive manufacture of large scale metal structures[J]. *Residual Stresses 2016: ICRS-10*, 2017, 2: 455.
- 32 Chiumenti M, Cervera M, Dialami N, et al. Numerical modeling of the electron beam welding and its experimental validation[J]. *Finite Elements in Analysis & Design*, 2016, 121:118-133.
- 33 Cervera M, Agelet de Saracibar C, Chiumenti M, COMET: Coupled mechanical and thermal analysis. Data input manual, version 5.0, technical report IT-308, (2002). <http://www.cimne.upc.edu>.
- 34 GiD: the Personal Pre and Post-Processor (2002) CIMNE, Technical University of Catalonia, <http://gid.cimne.upc.edu>.
- 35 Parry L, Ashcroft I A, Wildman R D. Understanding the effect of laser scan strategy on residual stress in selective laser melting through thermo-mechanical simulation[J]. *Additive Manufacturing*, 2016, 12: 1-15.
- 36 Szost B A, Terzi S, Martina F, et al. A comparative study of additive manufacturing techniques: Residual stress and microstructural analysis of CLAD and WAAM printed Ti-6Al-4V components[J]. *Materials & Design*, 2016, 89:559-567.
- 37 Cao J, Gharghoury M A, Nash P. Finite-Element Analysis and Experimental Validation of Thermal Residual Stress and Distortion in Electron Beam Additive Manufactured Ti-6Al-4V Build Plates[J]. *Journal of Materials Processing Technology*, 2016, 237:409-419.
- 38 N. Hoye, H.J. Li, D. Cuiuri, et al., Measurement of residual stresses in titanium aerospace components formed via additive manufacturing, *Materials Science Forum* vol. 777, Trans Tech Publications, 2014, pp. 124-129.
- 39 Setien I, Chiumenti M, Veen S V D, et al. Empirical methodology to determine inherent strains in additive manufacturing[J]. *Computers & Mathematics with Applications*, 2018.
- 40 Michaleris P, Zhang L, Bhide S R, et al. Evaluation of 2D, 3D and applied plastic strain methods for predicting buckling welding distortion and residual stress[J]. *Science & Technology of Welding & Joining*, 2006, 11(6):707-716.